Learning Fast and Slow: Increased cortical plasticity leads to memory interference and enhanced hippocampal-cortical interactions

Authors: Irene Navarro-Lobato[1]*, Adrian Aleman-Zapata[1], Anumita Samanta[1], Milan Bogers[1], Shekhar Narayanan[1], Abdelrahman Rayan[1], Alejandra Alonso[1], Jacqueline van der Meij[1], Mehdi Khamassi[2], Zafar Khan[3], Lisa Genzel[1]*

Affiliations:

[1]Donders Institute for Brain, Cognition and Behaviour, Radboud University, Postbus 9010 6500GL Nijmegen

[2]Institute of Intelligent Systems and Robotics, CNRS, Sorbonne Université, F-75005 Paris, France.

[3]Laboratory of Neurobiology, CIMES, University of Malaga, Campus Teatinos s/n, Malaga 29010, Spain

*Corresponding author. Lisa.Genzel@donders.ru.nl, ire_nl@hotmail.com

Summary

Our brain is continuously challenged by daily experiences. Thus, how to avoid systematic erasing of previously encoded memories? While it has been proposed that a dual-learning system with "slow" learning in the cortex and "fast" learning in the hippocampus could protect previous knowledge from interference, this has never been observed in the living organism. Here, we report that increasing plasticity via the viral-induced overexpression of RGS14414 in the prelimbic cortex leads to better one-trial memory, but that this comes at the price of increased interference in semantic-like memory. Indeed, electrophysiological recordings showed that this manipulation also resulted in shorter NonREM-sleep bouts, smaller delta-waves and decreased neuronal firing rates. In contrast, hippocampal-cortical interactions in form of theta coherence during wake and REM-sleep as well as oscillatory coupling during NonREM-sleep were enhanced. Thus, we provide the first experimental evidence for the long-standing and unproven fundamental idea that high thresholds for plasticity in the cortex protects preexisting memories and modulating these thresholds affects both memory encoding and consolidation mechanisms.

Introduction

Since patient H.M.[1] we know that memories are supported in the brain by a dual-learning system, but why this is the case remains unclear. Initially memories are stored in the hippocampus via synaptic changes in this more plastic brain area, known as the "fast learner" [2]. Later during sleep these hippocampal representations support reactivations of recent memories in the neocortex, the "slow learner" in the brain. Neocortical synapses are less plastic and therefore are thought to change only a little on each reinstatement. Therefore, remote memory is based on over time accumulated neocortical changes. Computational models testing why we have a dual-learning system have proposed that the neocortex learns slowly to discover the structure in ensembles of experiences [2-4]. Further, the hippocampus would then still permit rapid learning of new items without disrupting this structure and therefore the dual system would protect our memories from interference, when new memories would overwrite existing ones without the dual system. Although these theories provides remarkable insights about learning and knowledge extraction, they remains computational models with – until now – no direct experimental support, due to the lack of a valid behavioral paradigms that enable examining structured knowledge extraction in rodents as well interference effects.

To test if naturally restricted plasticity in the neocortex protects from memory interference, we artificially increased plasticity in the prelimbic cortex via the overexpression of an established plasticity-enhancer called regulator of G protein signaling 14 of 414 amino acids (RGS14414)[5,6]. The overexpression of RGS14414 is known to lead to increased BNDF and dendritic branching in the targeted area[5,6] and thereby increase plasticity locally. This increased local plasticity makes memories, that usually would not be retained, last longer and can rescue memory-deficits accompanying aging or diseases [7-9]. However, until now, the prefrontal cortex had not been targeted and it remained unknown how increasing plasticity would affect previously acquired knowledge. We combined this plasticity manipulation in the prefrontal cortex with a novel behavioral task – the Object Space task [10] – that allows the testing of semantic-like as well as simple memories in rodents.

We show that increased cortical plasticity leads to better one-trial memory performance. However, we observed that such enhanced fast learning is associated with impaired semantic-like, cumulative memories. In alignment with these findings, pharmacological experiments confirmed that these results were an outcome of local plastic changes in the prelimbic cortex. Next, we assessed the learning rate by devising a computational model and this model revealed that an increased learning rate in the intervention group augmented the influence of recent in contrast to remote memories on behavior. Finally, electrophysiological experiments showed that increased plasticity leads to 1) less NonREM sleep and smaller delta waves, 2) more neurons with slower firing rates, 3) increased hippocampal-cortical connectivity measured in theta-coherence, delta-spindle-ripple coupling and increased granger causality during ripple events and 4) off-target changes in hippocampal ripples.

Results

Increasing cortical plasticity leads to more memory interference

Prelimbic plasticity was increased by the overexpression of RGS14414[5-9] (Fig. 1A, B) and initially two behavioral experiments were performed using the Object Space task [10]. In this task the condition Overlapping tests for the extraction of an underlying structure across five training trials, while the Stable condition tests for the simple memory of the last experience (Fig. 1C). In both experiments, we examined the effect of an interference trial 24h after initial training, with object configurations violating previously trained rules, on a test trial 48h later (Fig. 1D). The design was such that in the Overlapping condition remembering the training resulted in positive discrimination indices at test, in contrast the interference would lead to 0 or negative values. In the control condition Stable remembering both the training or the interference would result in positive discrimination indices.

At the test trial conducted after interference, RGS14-overexpressing animals exhibited higher discrimination indices in the Stable condition (Fig. 1D, $p < 0.05$) but lower in the Overlapping condition ($p < 0.01$) in comparison to controls. The results in the Overlapping condition emphasize that in controls cumulative memory expression was protected from interference, but after increasing plasticity in the cortex interference effects were observed. Further, the simple memory in the Stable condition did not last until test in controls, however after increasing plasticity the memory lasted longer.

To show that these effects were a result of the interference, we conducted three control experiments. Firstly, we performed a behavioral control, in which animals did not experience the interference trial. Secondly, we performed a pharmacological control, in which animals did experience the interference, but any subsequent plasticity-related changes were inhibited in the cortex via the infusion of anisomycin, a protein synthesis inhibitor. In these experiments RGS14-overexpressing animals showed discrimination indices comparable to controls emphasizing the determinant role of the interference trial in producing opposite outcomes. Thirdly, we added an additional control, in which animals did not receive pretraining on the Object Space Task conditions, but instead were only exposed to an object configuration for one-trial. When tested 48h later, increased cortical plasticity led to an enhanced one-shot memory performance (Fig. 1E, $p < 0.05$).

Together, the behavioral and pharmacological results show that increasing cortical plasticity with RGS14-overexpression caused larger interference effects in a semantic-like memory task. Increased interference in this case was due to better memory for one-trial experiences and local changes in the prelimbic cortex. Thus, our experimental results verify for the first time the hypothesis that lower cortical plasticity is critical to protect previous knowledge from interference effects.

Memory interference is due to a higher learning rate

To characterize the build-up of a memory trace and its expression in the Object Space Task, we previously developed [10] a computational model that progressively learns place–object associations and makes decisions about which proportion of time to spend exploring each object in order to minimize uncertainty about these place–object associations. The model employs two parameters: a learning rate α, which determines the balance between recent and remote memories, and a parameter β, which determines the balance between neophilic (preference for more novel object location) and neophobic (aversion for more novel object location) exploratory behaviors. Here, we fitted our model on the behavioral data-set to find for each individual subject the values of the model parameter set α and β that best fit the data. There was no difference in memory expression (β). However, RGS14-overexpressing animals had systematically higher learning rate (α) values (Fig. 1F, $p < 0.05$). This indicates that exploration behavior in RGS14-overexpressing animals was driven more by recent than remote memories in contrast to controls.

Thus, the modelling results show that increasing cortical plasticity with RGS14-overexpression caused larger interference effects in a semantic-like memory task due to a higher learning rate.
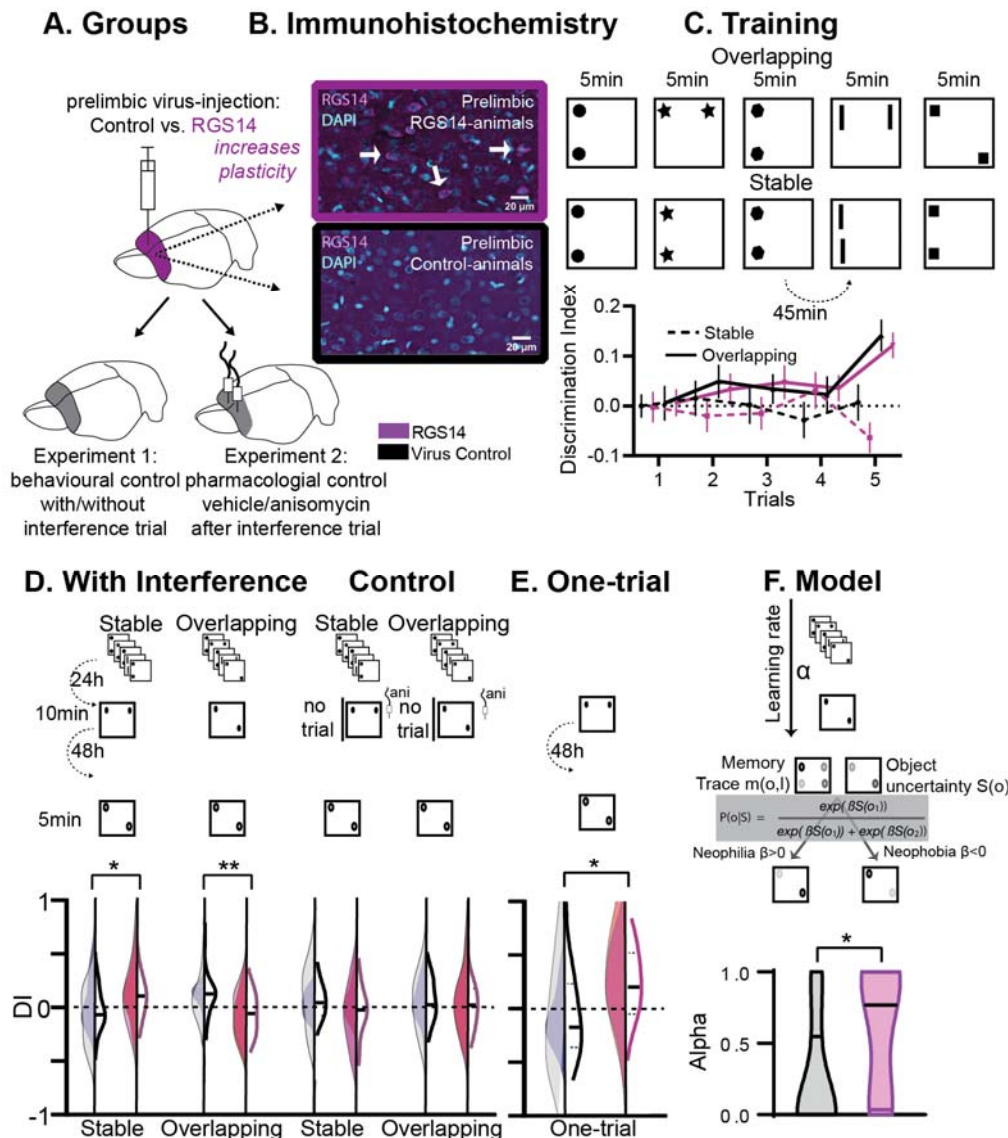
Fig.1 Behavioral Experiments: A. Half the animals were injected with a lentivirus for the overexpression of RGS14414 increasing plasticity in the prelimbic cortex, the other half had a control virus. These animals were included in either Experiment 1 (behavioral control), or were implanted with canula to the prelimbic cortex for Experiment 2 (pharmacological controls, total n=65 with n=16-17 per experimental group). **B.** Immunohistochemistry for RGS14 expression in treated and control animals (purple, cyan DAPI staining). **C.** Object Space Task training contains five trials with 45min inter-trial-intervals. In Overlapping one location always contains an object, while the other object moves each trial. In Stable the configuration always remains the same. Discrimination Index (exploration time moved-not moved/sum) over training trials show slowly rising discrimination in Overlapping and not Stable with preference for the less often used locations especially in the 5th trial as expected [10] 9DI interference and exploration times see Fig. S1). **D.** 24h after training animals had an interference trial (10min, different and same configuration as last training trial for Stable and Overlapping respectively) followed by a test trial another 48h later (again different and same configuration as interference trial for Stable and Overlapping respectively). In the controls (right side) for Experiment 1 there was no interference and in Experiment 2 animals were infused with anisomycin after the interference trial. There was a significant interaction where interference had the opposite effect in each condition according to virus manipulation (rmANOVA with condition, interference/drug, experiment, virus; cond*int/drug*virus $F_{1,61}=13.2$ p<0.001; stable with interference $t_{63}=2.1$ p=0.039, overlapping with interference $t_{63}=3.1$ p=0.003, other p>0.12). **E.** One-trial control followed 48h later by test, RGS14-overexpressing animals performed better than controls ($t_{30}=2.2$ p=0.037). **F.** Model-fitting show that RGS14-overexpressing animals have a higher learning rate α (KS-D=0.46 p=0.044). Control grey, RGS-overexpressing purple, lighter shades experiment 1, darker shades experiment 2, *p<0.05, **p<0.01

Increased cortical plasticity results in shorter NonREM bouts and smaller delta-waves

Sleep is supposedly the price the brain pays for plasticity [11,12]. The idea is that during a waking episode, learning statistical regularities about the current environment requires strengthening connections throughout the brain. This increases cellular needs for energy and supplies, decreases signal-to-noise ratios, and saturates learning. Therefore, subsequently during sleep, previous waking activity would lead locally to larger delta-waves (1-4Hz) and spontaneous activity during these oscillations in NonREM sleep should renormalize net synaptic strength and restore cellular homeostasis [13].

To test this, after viral-injection rats were implanted with hyperdrives containing 16 tetrodes targeting the hippocampus and prelimbic cortex (Fig. 2). We recorded neural activity during training as well as sleep in the Object Space task (OS) and compared this to a home cage control (HC). Surprisingly, RGS14-overexpressing animals showed less NonREM sleep (p<0.05, Fig. 2C), which can be attributed to shorter bout lengths (p<0.0001, Fig. 2D). These animals also presented with smaller amplitude delta-waves (p<0.0001). In controls, we did observe that delta-waves occurred more after learning (OS vs HC, p<0.0001, Fig. 2E) and that their amplitude (p<0.0001) increased while their intrinsic frequency decreased (Fig. S3A). These homeostasis effects in amplitude and intrinsic frequency after learning were also seen in RGS14-overexpressing animals (both p<0.0001).

In sum, in controls we could confirm the proposition that learning and therefore plastic changes lead to a homeostatic response with increases in delta wave activity. However, we show that artificially increasing plasticity in the prelimbic cortex does not lead to an enhancement of this effect. Instead, we observed the opposite, where RGS14-overexpressing animals show less NonREM sleep and smaller delta waves.

More neurons with slower firing rates after plasticity-increase

It has been previously proposed that slow-firing neurons are more plastic than fast-firing ones[14]. Thus, next, we focused on neuronal firing of individual neurons in the prelimbic cortex. We first determined the firing rate of each neuron during task performance and noticed that RGS14-overexpressing animals showed more neurons with low firing rates (p<0.0001, Fig. 2F). When splitting neurons in controls into pentiles according to their firing rate and applying the same margins to RGS14-overexpressing animals, the two lowest firing rate groups represented 40% of the neurons in controls but 75% in RGS14 (p=0.0005, Fig. 2G).

Moving to neuronal firing during sleep, only faster-firing neurons showed decreases in firing rate across different wake and sleep states (Fig. S3B) and this was the same for both groups. Spikes were less phase-locked to the slow oscillations in RGS14-overexpressing animals, which was seen for all firing rate groups (Fig. 2H, p<0.0001). However, faster-firing neurons contributed the most spiking activity to the upstate and with a decrease of these neurons in RGS14, these animals presented less spikes in the

upstate. This decrease in upstate activity likely underlies the decrease in delta-wave amplitude.

To summarize, RGS-overexpressing animals had more prelimbic neurons with slower firing rates. These results provide the first causal evidence that increasing synaptic plasticity shifts the neural firing towards the slow firing end of the neural firing spectrum. Furthermore, because it is the faster-firing neurons that dominate upstate spiking activity and therefore delta amplitude, the slowing of firing rates in the more plastic neurons is most likely the cause of the smaller delta waves seen in these animals.
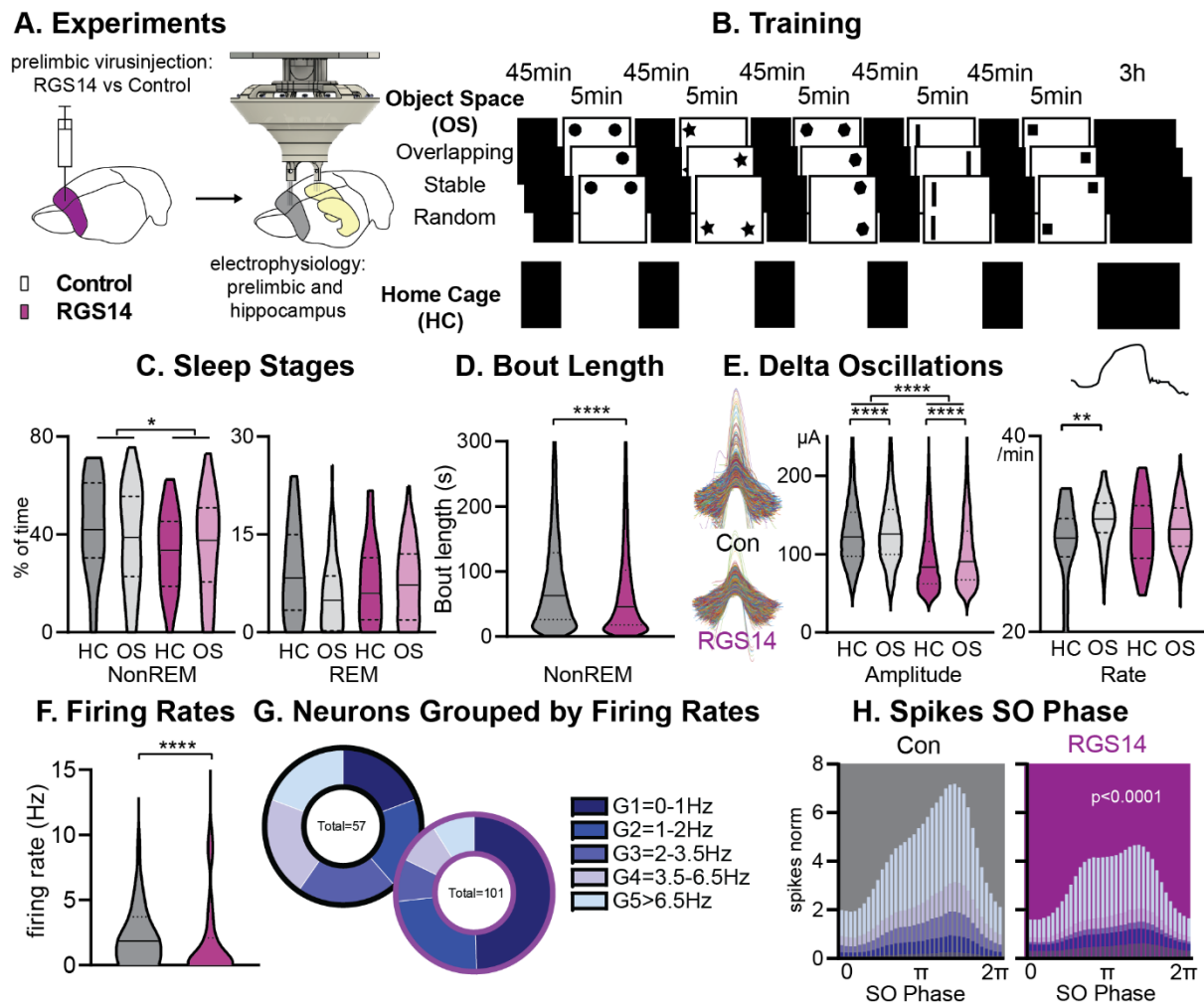
Fig.2 Sleep and Firing Rates: A. Animals received RGS14 overexpressing (n=4) or control (n=4) virus and were implanted with a hyperdrive (10 tetrode prelimbic, 6 tetrodes hippocampus) three weeks later. **B. A**nimals ran the three conditions of the Object Space Task (OS, Stable and Overlapping as described above, Random with constantly moving objects) and a home cage control (HC, same structure of the day but remained awake in recording box during trial periods). **C.** Controls had more NonREM sleep (KS-D=0.17 p=0.05) and no change in REM sleep (KS-D=0.15 p=0.12). **D.** NonREM bout length was longer in controls (KS-D=0.11 p<0.0001). **E.** Delta oscillations had higher amplitude in controls (KS-D=0.34 p<0.0001). In controls amplitude (KS-D=0.04 p<0.0001) and rate (KS-D=0.11 p=0.007) increased after OS, in RGS14-overexpresssing animals only amplitude increased (KS-D=0.07 p<0.0001). **F.** RGS14-overexpresssing animals had more neurons with lower firing rates (KS-D=0.36 p<0.0001)**. G.** Division of neurons according to their firing rates (Chi-square$_4$=20.13 p=0.0005). **H.** Spikes were less phase locked to the slow oscillation phase (circ stats p<0.0001 for each neuron group) and less G4-5 neurons led to less spikes during the upstate in RGS14. Control grey, RGS-overexpressing purple, darker shades home cage (HC), lighter shades Object Space Task (OS), *p<0.05, **p<0.01,****p<0.0001

Increased hippocampal-cortical connectivity during wake and sleep

Interactions between the hippocampus and cortex are critical during encoding as well as consolidation of memories[15] (Fig. 3A). During wake as well as REM sleep these interactions take place in the theta domain and can be measured in theta coherence [16]. In NonREM sleep, they can be captured in the coupling of cortical delta and spindle oscillations with hippocampal ripples [17]. Different types of interactions between these three oscillations have been reported; interactions between two oscillations such as delta followed by spindle [18], delta followed by ripple [19], ripple followed by delta [20], and spindles with a ripple in their troughs [21], but also three-oscillation interactions such as delta followed by spindle with a ripple in the trough [22], delta followed by ripple then spindle [17], ripple followed by delta and then spindle [20]. Interestingly, RGS14-overexpressing animals presented with higher hippocampal-cortical theta coherence during both task and REM sleep (Fig. 3B p<0.001) as well as increased occurrences of all types of NonREM oscillatory coupling (Fig. 3C p<0.001). In controls, we observed an experience-dependent increase (HC vs OS) in theta coherence (p<0.05) as well as NonREM oscillatory coupling rate (p<0.001, also single spindle rate Fig. S3), confirming the proposed association of these events to learning. This experience-dependent change was absent in RGS14.

Therefore, we could show that increased cortical plasticity led to increased cross-brain interactions during wake and sleep, emphasizing that decreased interactions and decoupling of the cortex from the hippocampus enables the protection of older, cortical memory representations. Further, these findings also highlight that hippocampal-cortical interactions can be regulated top-down by the cortex and not only by other neuromodulating brain areas or the hippocampus as previously assumed.
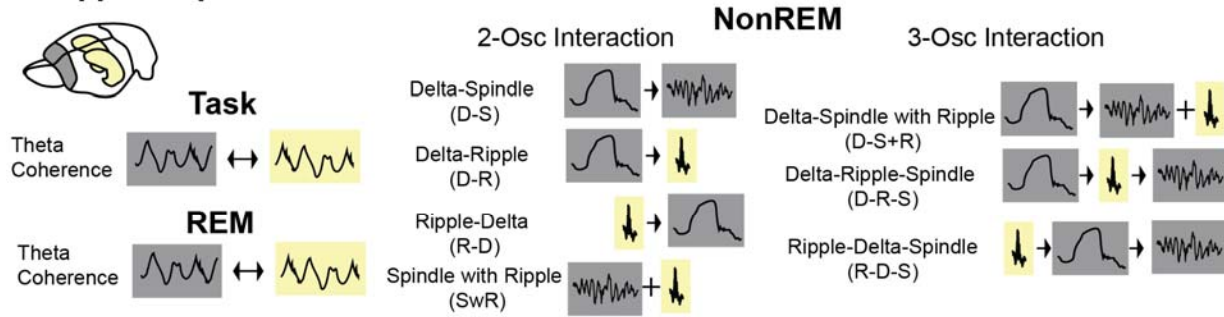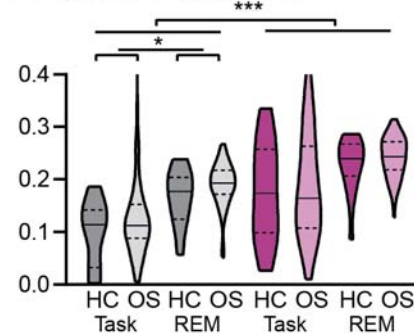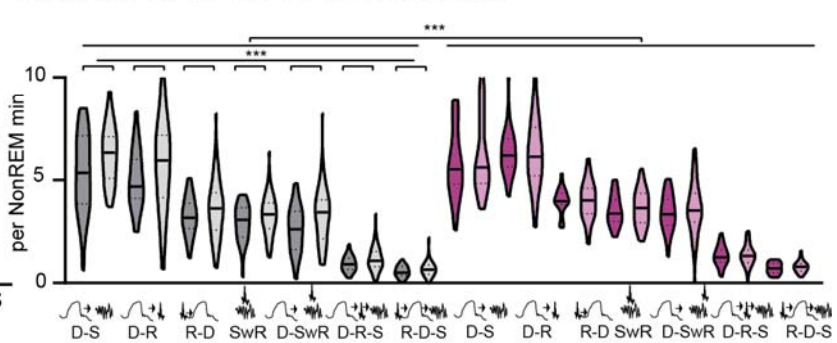
Fig. 3 Hippocampal-Cortical interactions: **A.** Brain area interactions are known in Task and REM as theta coherence[16], in NonREM as oscillatory coupling. **B.** RGS14 showed higher theta coherence (treatment $F_{1,285}=31.8$ $p<0.001$). Only controls showed higher coherence after learning (controls OS vs HC $F_{1,144}=5.2$ $p=0.024$, RGS14 OS vs HC $F_{1,141}=0.6$ $p=0.44$). **C.** RGS14 showed generally higher rates of oscillations sequences (treatment $F_{1,856}=18.7$ $p<0.001$), but only in controls could a learning-dependent increase be observed (controls OS vs HC $F_{1,420}=12.3$ $p=0.001$, RGS OS vs HC $F_{1,436}=1.3$ $p=0.25$). Control grey, RGS-overexpressing purple, darker shades home cage (HC), lighter shades Object Space Task (OS), *p<0.05, **p<0.01, ***p<0.001, ****p<0.0001
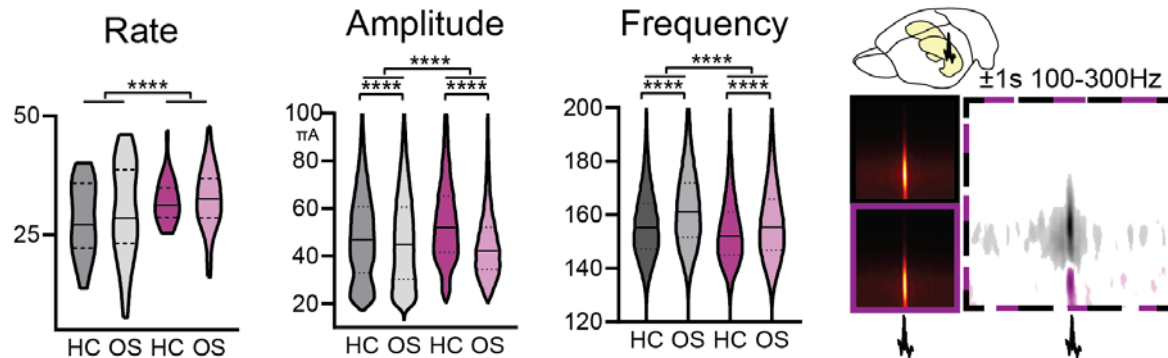
Increasing cortical plasticity leads to changes in hippocampal ripples

Next, we focussed on the hippocampal ripple oscillation in NonREM sleep, which is linked to memory reactivation, and therefore is suggested to be a key player in the memory consolidation process [14,23,24]. Increased cortical plasticity led to more, larger and slower ripples (Fig.4A all p<0.0001). Further, learning in comparison to home cage led to a decrease in ripple amplitude and increase in frequency in both animals' groups (each p<0.0001). In RGS14 ripples were less phase-locked to the slow oscillation (p<0.0001) and cortical delta power around ripples was decreased in comparison to controls (Fig.4B). Surprisingly, granger values around ripples measuring directional connectivity were higher in RGS14-overexpressing animals for Prl→Hpc in the delta frequency range (1-4Hz) and in the theta/beta range (5-20Hz) for Hpc→Prl (Fig.4B). The excitatory output of hippocampal ripples can lead to a neuronal response in the cortex [25]. This response was larger in controls in comparison to RGS14 (Fig. 4C p<0.001) because the average activity of ripple responsive neurons was higher (p<0.05).
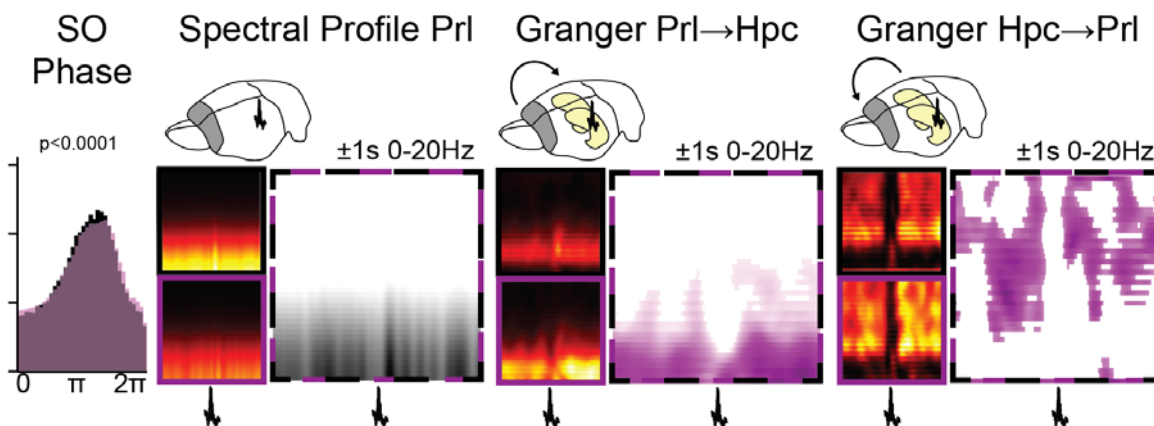
In sum, increased cortical plasticity also influenced the hippocampal ripple oscillation, ripples became larger, more numerous and the corresponding information flow and cortical neural response was attenuated. Our results imply that there is an important top-down, cortical influence on this oscillation beyond the known local hippocampal mechanisms.
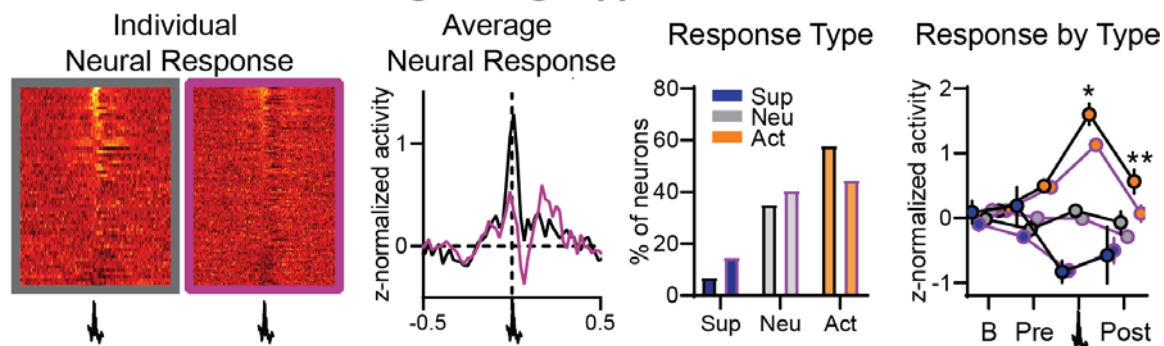
Fig. 4 Ripples: A. RGS14-overexpressing animals showed changes in ripple rate, amplitude, and frequency (rate KS-D=0.33 p<0.0001, amplitude KS-D=0.13 p<0.0001, frequency KS-D=0.13 p<0.0001). In both groups OS led to a decrease in amplitude and increase in frequency (vehicle KS-D=0.06 p<0.0001, RGS KS-D=0.25 p<0.0001). On the right hippocampal (Hpc) spectral profile 1s before and after the ripple in the 100-300Hz range (black Con, purple RGS, dotted Con vs RGS with statistically significant contrast with pixel-based correction for multiple comparison, grey con higher, purple RGS14 higher). **B.** Ripples showed less slow oscillation (SO) phase locking in RGS (phase lock circ stat. p<0.0001), which was also reflected in decreased delta power around the ripple (Prelimbic PrL spectral profile 1s before and after the ripple in the 0-20Hz range). Time-frequency granger analysis showed higher delta Prl→Hpc and higher theta/beta Hpc→Prl directional connectivity (black Con, purple RGS, dotted Con vs RGS with statistically significant contrast with pixel-based correction for multiple comparison). **C.** Neural firing during ripples in prelimbic cortex. From left to right: individual neuron response (each row one neuron) aligned to ripple (middle); average response across neurons (rmANOVA treat*time $F_{98,15288}$=2.7 p<0.001); neurons were categorized into types with ripple suppressed (blue), ripple neutral (grey) and ripple active (orange, Chi-square 3.46 p=0.18); for each types the response at baseline (200-120ms before ripple), pre-ripple (120ms-40ms before ripple), during ripple (40ms before – 40ms after ripple peak), and post-ripple (40ms-120ms after ripple, rmANOVA treat*ripple response $F_{2,162}$=3.2 p=0.043, post-hoc RGS vs. Con active neurons during p=0.015 and after p=0.003). Control grey, RGS-overexpressing purple, darker shades home cage (HC), lighter shades Object Space Task (OS), *p<0.05, **p<0.01, ***p<0.001, ****p<0.0001

Discussion

By increasing plasticity in the prelimbic cortex via the overexpression of RGS14 and combining this with behavioural, pharmacological, computational, and electrophysiological approaches, we tested the long-standing but unproven idea of a slow- and fast-learner in the brain. Our data strongly suggests that restricted cortical plasticity is needed to protect memories from interference, the first experimental confirmation of Marr and McClellands ideas that have fundamentally shaped our concepts of memories. Increasing plasticity enhanced one-trial memory, increased memory interference in our semantic-like memory paradigm and learning-rate in our modelling approach. Signatures of cross-brain connectivity – hippocampal-cortical theta coherence, NonREM oscillation coupling, granger causality analysis of ripple events – were all increased after our plasticity manipulation. However, experience-dependent increases, that were present in controls, were lacking in RGS14 animals. Increased plasticity in the prelimbic cortex also changed hippocampal ripple oscillations, arguing for a top-down control of the cortex on this oscillation.

Interestingly, while most signatures of learning were increased, some seemed to break down. Contrary to predictions by the SHY hypothesis[11,12], delta waves were smaller in RGS14-overexpressing animals. The cause is likely the general decrease in firing rates accompanying increased plasticity. Slower-firing neurons were less phase locked to the slow oscillation and less neuronal firing in the upstate led to smaller delta waves. It has been previously proposed that slow-firing neurons are more plastic than fast-firing ones [14]. The current evidence, however, was mainly correlational. Our results provide the first causal evidence that increasing synaptic plasticity shifts the neural firing towards the slow firing end of the neural firing spectrum. Furthermore, our results highlight the complex interaction of proposed plasticity-related mechanisms present in firing-rates and sleep oscillations.

While RGS14-overexpressing animals had more ripples and cortical-hippocampal interactions, the response of cortical neurons to ripples remained lower than in controls. The current prevalent view on hippocampal ripple oscillations is that they are essential for memory consolidation. Furthermore, it is believed that they are generated mainly as an outcome of the local synaptic interactions within the hippocampus inducing changes in several cortical areas and supporting the broadcasting of information from the hippocampus to the cortex[23]. Our results imply that there is an important top-down, cortical influence on this oscillation beyond the known local hippocampal mechanisms. Furthermore, and in alignment with existing results, it shows that hippocampus doesn't reactivate random incoming sensory information, instead it orients itself to the previous knowledge acquired by the cortex[26,27].

To conclude, we could show that increasing plasticity in the prelimbic cortex enhances the ability to retain one trial information but this negatively impacts abstracted, cumulative memory representations and the ability to distinguish learning experiences, confirming long-standing but unproven memory system theories. Furthermore, changes

330 in cortical plasticity affect neuronal firing rates, hippocampal-cortical connectivity, cortical

331 delta waves and hippocampal ripples.

332

333

MATERIALS AND METHODS

Study design

A total of 72 rats were used in this experiment: 64 in the behavioral experiment and 8 in the electrophysiological recordings. In each case animals were first extensively handled for multiple days (at least 3) until they did not flinch when the experimenter touched them (see handling videos on www.genzellab.com). Next, all animals underwent viral-injection surgery (see below), half the animals received RGS14$_{414}$-lentivirus while the other had a vehicle (empty) lentivirus. In addition, 32 animals also received pharmacological canula's targeting prelimbic region during this surgery (16 vehicle, 16 RGS). These and the other 32 behavioural animals had a 2-week surgery recovery and then went on to do the habituation as well as training in the Object Space Task (all conditions counterbalanced within animal). The 8 electrophysiology animals (4 vehicle, 4 RGS) received a second surgery three weeks after the first one, for hyperdrive implantation. During 2–3-week surgery recovery, tetrodes were slowly lowered to target area before the animals also had habituation and training in the Object Space Task.

All data will be available on the Donders Repository.

Animals

Three-month-old male Lister Hooded rats weighing between 300-350 g at the experiment start (Charles Rivers, Germany) were used in this study. Rats were pair-housed in conventional eurostandard type IV cages (Techniplastic, UK) in a temperature-controlled (20 + 2 ºC) room following a 12 h light/dark cycle with water and food provided *ad libitum*. After lentiviral surgical intervention, animals were single-housed for two days and paired with their cage mates after recovery in rat individually ventilated cages (IVC; Techniplastic, UK). Animals were maintained in their IVC in a barrier room for 14 days before downscaling them to conventional housing conditions. After hyperdrive implantation, rats were single-housed in until the end of the experiment. A total of 72 rats were used in this experiment: 64 in the behavioral experiment (n=16 per group, RGS14$_{414}$, vehicle, across two cohorts of 8-8 animals each; and n=16 per group RGS14$_{414}$-pharma, vehicle-pharma group across two cohorts of 8-8 animals each), and 8 in the electrophysiological recordings (n=4 per treatment, RGS14$_{414}$, and vehicle, split one animal per treatment across four cohorts). The behavioral experiments and electrophysiological recordings were performed during the light period (between 9:00-18:00).

All animal procedures were approved by the Central Commissie Dierproeven (CCD) and conducted according to the Experiments on Animals Act (protocol codes, 2016-014-020 and 2016-014-022).

RGS14$_{414}$-lentivirus

The RGS14$_{414}$- and vehicle-lentivirus solutions (1.72 x 10^7 CFU/ml and 2.75 x 10^6 CFU/ml respectively) were prepared and provided by Dr. Zafaruddin Khan at the University of Malaga (Malaga, Spain)[28][29]. Briefly, the RGS14$_{414}$ gene (GenBank, AY987041) was cloned into the commercial vector p-LVX DsRed Monomer-C1 (Clontech, France) using DNA recombinant technology. Then, both non-replicant RGS14$_{414}$- and vehicle-lentivirus (empty vector) were prepared and titered using the Lenti-XTM (Clontech, France) according to the manufacturer's instructions.

The animal's procedures related to the non-replicant lentiviral solution were approved and carried out in compliance with institutional regulation.

Tetrode hyperdrive

A customized lightweight tetrode micro-drive was manufactured to implant 10 and 6 movable tetrodes in the prelimbic cortex and hippocampus (HPC), respectively [30-32]. Two separate bundles of #33 polyimide tubes (Professional Plastics,) were prepared: one of 2 columns x 5 rows for prelimbic cortex and 3 X 3 for HPC. The bundles were fixed first to the customized 3D printed cannula and then into the customized 3D printed body drive. The 3D printed cannula was designed according to the Rat Brain Atlas in Stereotaxic Coordinates [33] for the correct placement of the bundles in the areas of interest. Inner tubes (#38 Polyimide

tubes; Professional Plastics) were placed inside the outer tubes and glued to the shuttle, which moves through the body spokes thanks to an inox steel screw and a spring CBM011C 08E (Lee spring, Germany). A total of 16 tetrodes were built, twisting four 10 cm polyimide-insulated 12 µm Nickel-Chrome wires (80 turns forward and 40 turns reverse) (Kanthal Precision, Florida) and fused by heat. Tetrodes were loaded in the inner tubes, and their free ends were connected to a customized 64 channels, 24 mm round electrode interface board (EIB) using gold pins (Neuralynx). Previously, 2 NPD dual row 32 contact connectors (Omnetics) had been attached to the EIB. The tetrode tips were cut using fine sharp scissors (maximum length 3.5 mm and 3 mm for prelimbic cortex and HPC, respectively) and fixed to the inner tubes in the upper part. Tetrode tips were clean in distilled water and gold-plated (gold solution, Neuroalynx) using NanoZ software to lower their impedance to 100–200 kΩ and improve the signal-to-noise ratio. The tetrode tips were hidden at the same level as the bundle. The whole drive was covered with aluminum foil connected to the ground to reduce the electrostatic interference during the recordings. The bottom of the micro-drive was deepened in 70 % ethanol for 12 hours before brain implantation.

Stereotaxic surgeries
Lentivirus injection

Lentiviral solutions were infused in the prelimbic cortex using stereotaxic surgery under biosafety level 2 conditions. The coordinates of the prelimbic cortex injection site were +3.2 mm AP, +/-0.8 mm ML from Bregma, and -2.5 mm DV from dura mater, according to The Rat Brain Atlas from Paxinos and Watson [33]. The procedure was carried out under isoflurane inhaled anesthesia. Unconsciousness was induced at 5 % isoflurane + 1 l/min O_2 and maintained at 1.5-2 % isoflurane +1 l/min O_2. A 0.8 mm diameter craniotomy was drilled above the target area in each hemisphere. The DV dura mater coordinate was measured before performing the durotomy.
A 30 G dental carpule connected to a 10 µl Hamilton and an infusion pump (Micro-pump, WPI) was slowly inserted into the brain target area (0.2 mm/min). A total volume of 2 µl of the lentiviral solution was infused at 200 nl/min. After 5 minutes of diffusion, the needle was removed, and the incision was sutured.

For the anisomycin infusions, 32 animals were implanted with a 26 G bilateral guide cannula (3 mm length and 1.6 mm inter-cannula distance; Plastic1 Technology, USA) above prelimbic cortex (AP +3.2 mm, ML +/- 0.8 mm from Bregma and DV -0.5 mm from dura mater [33]). Three supporting screws 1 mm X 3 mm were driven approx. 0.9-1 mm into the skull around the cannula. The bilateral cannula was slowly inserted into the brain target area (0.2 mm/min) after dura matter was removed. The whole structure was attached to the previously scratched skull by Metabond (Sun Medical, Japan) and simplex rapid dental cement (Kemdent, UK). The lentivirus infusions took place similarly as explained above, but using a 30 G bilateral internal cannula with a 2 mm projection length from the guide cannula (Plastic1 Technology, USA). The final DV coordinate was -2.5 mm from the dura mater. After 5 minutes of diffusion, the internal cannula was removed, the guide cannula was protected with a bilateral dummy cannula without projection and its cap.

Temperature, oxygen saturation, and blood pressure were monitored during the whole surgical procedure. Some eye cream (Opthosam) was applied to protect the corneas during the intervention. At the start and end of the surgery, 2 ml of 0.9% NaCl physiological serum was administered subcutaneously. As analgesia, animals were administered 0.07 mg/ml carprofen in their water bottles two days before and three days after surgery. Immediately before surgery, 5 mg/kg carprofen was sc injected. In addition, a mix of 4 mg/kg lidocaine and 1 mg/kg bupivacaine in a 0.9% NaCl physiological serum was administered sc locally in the head.

After the viral injection, animals were housed individually in rat IVC cages for 14 days. Their weights and status were monitored daily for the correct recovery of animals. Then, rats were pair housed with their previous cagemate and moved to conventional housing.

Tetrode hyper-drive implantation

Twenty-one days after viral infusion, a second stereotaxic surgery took place for tetrode micro-drive implantation in 8 animals. The procedure was similar as described above. In this intervention additionally, a prophylactic 10 mg/kg sc injection of Baytril antibiotic was administered at the beginning of the surgery. Two craniotomies (2x1 mm and 1x1 mm for prelimbic cortex and HPC, respectively) were drilled above the target areas on the right hemisphere. The coordinates for the upper left corner of each craniotomy were: AP +4.5 mm and ML -0.5 (prelimbic cortex) and AP -3.8 mm and ML -2 mm (HPC) from Bregma [33]. A ground screw (M1x3) was placed on the left hemisphere in the cerebellum (AP -11 mm, ML +2 mm from Bregma). In addition, six M1x3 mm supporting screws were driven and bound to the skull using Super-bond C&B dental cement (Sun Medical, Japan). Carefully, the durotomies were performed, and the brain's surface was exposed. Subsequently, the micro-drive was positioned on the brain's surface, and attached to the skull and the screws by simplex rapid dental cement (Kemdent, UK). Then, tetrodes were slowly screw-driven into the prelimbic area in prelimbic cortex (3 mm DV from brain surface) and the cortical layers above the HPC (1.5 mm DV from brain surface). The dorsal hippocampal CA1 pyramidal layer was reached progressively in the subsequent days.

Pharmacological infusion

Anisomycin (ANI) powder (Merck, Germany) was solved in 1 M HCl in 0.9% NaCl physiological serum, and the pH was adjusted with 10 µl of 5 M NaOH. Aliquots were prepared and stored at -20ºC until the moment of use. Immediately after the 24 h test in the object space task, animals were infused with 3 µl/hemisphere of a 25.6 µg/µl ANI solution or the solvent as control at 300 nl/min. An infusion pump and two 10 µl Hamilton syringes connected through a PE10 tube (Plastic1;) to a customized 30 G bilateral internal cannula with a 2 mm projection (Plastic1;) was used for the infusion. The internal cannula was carefully removed after 3 minutes of diffusion time, and the dummy and cap were placed back. All the animals from Experiment 2 received the infusion of both ANI and vehicle across different weeks for each experimental paradigm.

Object Space Task

The Object Space Task (OST) is a newly developed behavioral paradigm to study simple and semantic-like memories in rodents [34]. The task is based on the tendency of rodents to explore novel object-location in an open field across multiple trials. In these experiments, the OST took place as described previously [34] at least 21 days after the viral infusion when the effect of the RGS14$_{414}$ protein is observed [28,29]. Briefly, animals were handled for 5 consecutive days before and after surgery recovery. Then, rats were accommodated in the experimental room and habituated to the open field across 5 sessions (one per day). In the first session, animals explored the open field with their cagemate for 30 minutes. In the rest of the session, each individual freely explored the open field for 10 min. Two Duplo objects were included in the open field center in the last two sessions to facilitate a better exploration time in the subsequent task.

The OST consists of two phases: a training phase of 5 training trials in which animals are exposed to two identical objects (different across trials) for 5 minutes (45-55 min intertrial time); and a interference/test phase consisting of a single 10 min' trial performed 24 h and 72 h after training. In the stable condition, both object locations were fixed during the training trials, and one object location was moved during the interference and tests sessions. In the overlapping condition, one object location was fixed, and the other one moved across training trials. In the interference and test sessions, the same object-location pattern from the last training trial was repeated.

The open field was a wooden square 75 x 75 x 60 cm. For the task, but not for the habituation, we placed 2D proximal cues on the open field walls and 3D distal cues above the open field. The cues were changed in each experimental session. In addition, the open field base colors changed across task sessions (white, blue, green, brown). The objects used vary in material (plastic, glass, wood, and metal), size, and colors. For electrophysiological recordings, not plastic objects were used to prevent static interference. All

479 object bases were attached to 10 cm x 10 cm metal plates. Circular magnets were installed in the corners
480 underneath the open field floor to prevent object movements during exploration. The open field and object
481 surfaces were cleaned with 40% ethanol between trials to avoid odor biases.

482 Each trial was recorded using a camera above the open field. The object exploration time was
483 manually scored *online* using the homemade software '*Scorer32*'. The experimenter was blinded for
484 treatment and experimental conditions at the moment of scoring. Object locations and experimental
485 conditions were counterbalanced across treatments, individuals, and sessions.

486 For electrophysiological recordings, we run four cohorts of 2 animals each. Each cohort included one
487 vehicle- and one RGS14$_{414}$-treated animal, which performed the identical condition sequences with the
488 same object-location patterns. Object locations and experimental conditions were counterbalanced across
489 cohorts. Electrophysiological recordings took place during trials and rest periods (45 min before and 3 h
490 after both training and test; and 45 min intertrial time during the training). Therefore, two brown wooden
491 sleep boxes (40 x 75 x 60 cm height) with bedding material were placed next to the open field. Animals had
492 been accustomed to the sleep box for at least 3 h in each open field habituation session.

493 Rats involved in the electrophysiological recordings also performed two experimental control
494 conditions: homecage and random. The random condition was carried out as described previously [34], so
495 there was a lack of repetitive object location patterns across different trials. In the homecage, the animal
496 was recorded for 7 h and 10 min in the sleep box (a whole training session recording), and the experimenter
497 kept the rat awake for the equivalent trial times.

In vivo electrophysiology recordings

500 In vivo freely moving extracellular recordings were executed during the OST and the resting periods.
501 One session per experimental condition (homecage, stable, overlapping, and random) was carried out per
502 animal. The local field potential (LFP) and single-unit activity detected by the 64 channels were amplified,
503 filtered, and digitized through two 32 channels chip amplifier headstages (InstanTechnology) connected
504 through the Intan cables and a commutator into the Open Ephys acquisition box. The signal was visualized
505 using the open-source Open Ephys GUI (sample rate 30 kHz). In addition, the headstage contains an
506 accelerometer to record the movement of the animals.

Tetrode electrolytic lesions

509 After all the recording sessions, the tetrode-implanted animals received brain electrolytic lesions 48
510 h before the transcardial perfusion to identify the electrode tips placement. Thus, a current of 8 µA for 10 s
511 was applied in two wires per tetrode using the stimulator with the animal under isoflurane inhaled
512 anesthesia.

Histology

Brain processing

516 After data collection, animals had overdoses with 150 mg/kg sodium pentobarbital ip. Rats were
517 transcardially perfused first with 80 ml of 0.1 M phosphate-buffered saline pH 7.4 (PBS) and then with 250
518 ml of 4% (w/v) paraformaldehyde in 0.1 M phosphate-buffered pH 7.4 (PFA). After brain extraction, it was
519 immersed in PFA overnight at 4ºC. Then, the brains were rinsed in PBS 3 times for 10 min and
520 cryoprotected by deepening in 20 ml of 30% (w/v) sucrose, 0.02% (w/v) NaN$_3$ in PBS. Once brains sank
521 (after 2-3 days approx), they were frozen in dry ice and stored at -80ºC. Finally, 30 or 50 µm coronal
522 sections of target areas were obtained using the cryostat (SLEE medical, Germany), collected in 48-well
523 plates containing 0.02 % (w/v) NaN$_3$ PBS and stored at 4ºC.

Immunohistochemistry

526 The overexpression of rgs14$_{414}$ was checked by free-floating fluorescence immunohistochemistry.
527 First, the target sections were selected, rinsed in PBS, and incubated overnight at 4°C with the rabbit

polyclonal anti-RGS14 antibody (Novus biological, NBP1-31174; dilution 1:500). Then, the Alexa fluor® 488-conjugated goat anti-rabbit IgG (Life Technologies, A11008; dilution 1:1000) at room temperature for 2.5 h. Some drops of water-soluble mounting medium containing DAPI (Abcam, ab104139) were applied for 5 min before placing the coverslip. Leica fluorescense microscope (Leica DM IRE2) and camera were used to observe and photograph the samples.

Nissl staining

Coronal sections were AP sequentially mounted on gelatin-coated slides and incubated at 37 ºC overnight. Slices were hydrated first in 0.1 M PBS pH 7.4 and then in Milli Q water for 20 min each. Next, brain sections were stained in 0.7 %(w/v) acetate cresyl violet for 20 min and dehydrated in an increasing ethanol gradient (water for 3 min, 70% ethanol for 20 s, 96% ethanol+acetic acid for 45 s, 100% ethanol for 5 min). Lastly, the tissue was immersed in xylene for 15 min, and the coverslip was placed using some DePeX mounting medium drops. Cannula placement, infusion traces, or/and tetrode lesions were observed and photographed under a light field microscope (Leica DM IRE2) and a camera.

Sleep scoring

Different states (wakefulness, NonREM, REM, and Intermediate) were *off-line* manually scored using, *'TheStateEditor'* developed by Dr. Andres Grosmark at Dr. Gyorgy Buzsaki lab. One channel per brain area (Prelimbic cortex and HPC) was selected per animal. The frequency spectrograms and bandpass filtered LFP signal were computed per brain area, and the motion spectrogram. Using a 10 s sliding window, an experienced researcher created the hypnogram and 1 s epoch vector indicating brain states. The absences of movement in the motion spectrogram discriminate between wakefulness and sleep. During sleep periods, a dominant theta frequency in the dorsal hippocampus in the absence of spindles and delta waves indicated REM sleep. NonREM sleep was classified when slow oscillations were detected in the prelimbic cortex. The intermediate phase was defined as short transitional periods between NonREM and REM that show an increase in frequency in the prelimbic cortex and frequency similar to theta in the dorsal hippocampus. Microarousals were defined later on as periods of wakefulness $\leq$ 15 s within a sleep period.

Behavioral data analysis

Object Space Task.

The total exploration time was calculated as the sum of the time spent exploring both object locations. The discrimination index (DI) was computed by subtracting the familiar object location exploration time to the novel object location and dividing it by the total exploration time. A DI > 0 means a preference for the new object location and consequently memory from the previous episode. A DI = 0 shows no preference for either the new object location or the fixed one. DI<0 means a preference for the stable object location.

Model

The same computational model as in (Genzel et al., 2019) was used (see article for more detailed methods). In short, the model learns place-object associations and then translates this memory into an exploratory behavior: the objects that were stably found at the same location have a very low uncertainty and are thus either less attractive or more attractive (depending on the individuals) during exploration than objects found at changing locations (high uncertainty in place-object association). The source code of the computational model and model simulation/fitting procedures is available here: https://github.com/MehdiKhamassi/ObjectSpaceExplorationModel

The model employs two different parameters: a learning rate α, which determines the speed of memory accumulation; an inverse temperature β, which determines the strength and sign of memory expression during exploratory behavior.

A low learning rate α (i.e., close to 0) means that the model will need numerous repetitions of the same observation (i.e., in the Object Space Task, many trials observing the same place-object association) to properly memorize it. In contrast, a high learning rate α (i.e., close to 1) means that the model quickly memorizes new observations at the expense of old observations which are more quickly forgotten. As a consequence, with a low learning rate the exploratory behavior generated by the model will mostly reflect remote memories but not recent ones (semantic-like memory). Conversely, with a high learning rate, exploratory behavior in the model will mostly reflect recent memories but not remote ones (episodic-like memory).

Finally, an inverse temperature β close to zero means that the model does not strongly translate memories into object preferences for exploration, thus showing little object preference. In contrast, a high inverse temperature will mean that the model's exploratory behavior is strongly driven by differences in relative uncertainty between place-object associations. A high positive inverse temperature ($\beta > 0$) will result in neophilic behavior: the model spends more time exploring objects associated with high uncertainty (i.e., novelty or constantly changing location); a high negative inverse temperature ($\beta < 0$) will result in neophobic behavior: the model spends more time exploring objects with low uncertainty (stable/familiar objects).

The model was fitted to each mouse's trial-by-trial behavior using a maximum likelihood procedure described in (Genzel et al., 2019), and similar to state-of-the-art model fitting methods in cognitive neuroscience (Collins & Wilson, 2019). In brief, this model fitting process found the best parameter values for each subject that best explain the relative proportion of time spent exploring each object at each trial. The main operations of the model are summarized in **Figure 1F**. All model equations are described in [10].

Sleep architecture analysis

Macroarchitecture. The total sleep time (TST), total wakefulness time, and total time for different sleep states (NonREM, REM, and Intermediate) were computed per session on MATLAB. The average across sessions was calculated per rat, and the mean and SEM were computed per treatment. Additionally, the % of TST of NonREM time, REM time, and intermediate time were calculated for the 3 h recording post-training.

Microarchitecture. The distribution of bout duration per stage was computed per treatment. The bouts number and duration were calculated per resting period and state. Only bouts longer than 4 seconds were considered for the analysis. The 1 s epoch state vectors of each session were concatenated with the interleaved trial wakefulness. NonREM episodes were defined as consecutive NonREM bouts without considering microarousals. Sleep period was described as an event of sleep between wake events $\geq$ 300 s. Each sleep period could include several NonREM periods defined as NonREM episodes without considering microarousals, or NonREM episodes followed by transitional stages and/or sleep cycles defined as NonREM episodes followed by transitional states and REM or NonREM followed by REM. In sleep, periods can include quiet wakefulness < 300 s. The number of sleep periods and the average duration per treatment were calculated on MATLAB. Additionally, the count and duration of NonREM periods and sleep cycles were also computed per treatment.

Local field potential analysis
Signal preprocessing
For the following analyses, first a single channel was selected per brain area. For prelimbic cortex, the channel with the largest slow oscillations was chosen. For hippocampus, the channel closest to the pyramidal layer, which displayed noticeable ripples was selected. Both channels were originally acquired at a sampling rate of 30 kHz and to avoid working which such a high rate, the channels were filtered with a 3rd order Butterworth lowpass filter at 500 Hz to avoid signal aliasing and then downsampled to 1 kHz.

Theta coherence

Theta coherence was computed as the magnitude squared coherence using the *mscohere function in* MATLAB and a custom-written script that collected the downsampled data from different animals and study days. The magnitude squared coherence was calculated as follows:

$$Cxy(T) = \frac{|Pxy(T)|}{Pxx(T)Pyy(T)}$$

where Cxy is the magnitude coherence, Pxy is the cross spectral density of the hippocampal and prelimbic cortex signal, Pxx is the hippocampal signal, and Pyy is the prelimbic cortexsignal. The coherence analysis focused on two periods of interest namely, WAKE and REM periods. Since REM sleeping periods might occur several times over several sleeping cycles, REM periods from pre and posttrial sleep were first extracted and concatenated together before running the analysis. For both Wake and REM periods, the power and cross-power spectra were computed on overlapping time windows of 1 second with 80% overlap. Then, the theta coherence was computed as the average value over the theta frequency range (5-12 Hz) for the Object Space (Stable, Overlapping and Random) and home cage conditions.

Detection of spindles and delta waves

The downsampled prelimbic cortex channel (1kHz) was loaded and using a 3rd order Butterworth filter the signal was filtered to 9-20Hz for detecting spindles and to 1-6Hz for detecting delta waves. The NonREM bouts were then extracted from the filtered signal and concatenated. The functions FindSpindles and FindDeltaWaves from the Freely Moving Animal (FMA) toolbox http://fmatoolbox.sourceforge.net were modified and used to detect the start, peak and end of spindles and delta waves respectively. The optimal threshold was found for each animal by visually inspecting the detections and modifying the default parameters of the functions when needed. The results were saved as timestamps with respect to the concatenated NonREM signal in seconds. They were then used to find the timestamps with respect to the recorded signal. This process was repeated for pre and post trial sleep periods in study days pertaining to all animals in both treatment groups.

Ripple Detection

The downsampled channels (1kHz) of the hippocampal pyramidal layer were loaded and the NonREM bouts were extracted. Using a 3rd order Butterworth bandpass filter, the epochs of HPC signal were filtered to a frequency range of 100-300Hz. A custom MATLAB function was used for detecting the start, peak and end of the ripples by thresholding voltage peaks which lasted a minimum duration of 30 ms above the threshold. The start and end of the ripple were determined as half the value of the selected threshold. The standard deviations of concatenated NonREM bouts were computed individually for presleep and all post trials in a study day. The average of these standard deviations was calculated to find a single detection threshold per study day. An offset of 5 units was added to the threshold to reduce false positives. This was repeated for all study days pertaining to all animals in both treatment groups.

Oscillations characteristics

The traces of each event detected (ripples, spindles, delta waves) were extracted using the start and end timestamps obtained from the detectors. The traces of the events were filtered in their corresponding detection frequency band. Characteristics such as the amplitude and mean frequency were calculated for these filtered events using built-in and custom MATLAB functions. Namely, the amplitude of the events was calculated by computing the envelope of the filtered trace using a Hilbert transform. The absolute value of the result was taken and its maximum was found. The mean frequency of the filtered traces was computed using the meanfreq function of MATLAB.

Detection of oscillation sequences

The sequences between ripples, spindles and delta waves were counted in various combinations to study cortico-hippocampal coupling during NonREM sleep as done by Maingret et. al. [20] . The time difference between the peaks of these events was compared to a fixed duration to establish if there was a sequential relationship in the following combinations of oscillations: Delta-Spindle (D-S), Delta-Ripple (D-R), Ripple-Delta (R-D), Ripple-Delta-Spindle (R-D-S). For D-S a sequence was considered when the duration between events was between 100-1300 ms, for D-R it was 50-400 ms and for R-D it was 50-250 ms. To find R-D-S sequences, the results of R-D and D-S were compared to find delta waves preceded by a ripple and followed by a spindle. The results were saved as counts of each sequence for each post-trial.

Co-occurrence between ripples and spindles

The co-occurrence between ripples and spindles was computed by comparing the start and end timestamps of both events. To consider co-occurrence between a ripple and a spindle, either one of the following conditions had to be fulfilled. 1) A ripple had to start and end within the duration of the spindle. 2) One of the events had to start or end within the duration of the other. Given that more than one ripple can co-occur with the same spindle, we counted separately spindles co-occurring with spindles and spindles co-occurring with ripples.

Slow oscillation phase

The downsampled prelimbic cortex signal was filtered in the 0.5 to 4 Hz range using a 3rd order Butterworth bandpass filter and its Hilbert transform was computed to find the phase angle of slow oscillations in a range from 0° to 360°. The peaks of ripples and spindles were then used to find the corresponding slow oscillation phase. This same signal was later used to find the phase during spikes timestamps of cortical neurons.

Spectral analysis and Granger causality

A two-second-long window centered on each ripple peak was extracted from the hippocampus and the prelimbic cortex channels respectively. All ripples across animals and conditions were combined per treatment and their amplitude was computed by finding the maximum of their envelope computed with a Hilbert transform. The median ripple amplitude was calculated and the corresponding two-second-long windows of the 2000 ripples which amplitude was the closest to the median amplitude were included in the following analysis. A notch filter at 50 Hz was applied to the ripple-centered windows using the ft_preprocessing function from the Matlab-based Fieldtrip toolbox [35]. The Short-time Fourier transformation was calculated to detect the changes of spectral power in hippocampus and prelimbic cortex with respect to a time window of ± 1 second around each ripple. This was computed using the ft_freqanalysis function from Fieldtrip with a 100 ms Hanning window and time steps of 10 ms, for a frequency range from 100 to 300 Hz with a 2 Hz step for hippocampus and from 0.5 to 20 Hz with a step of 0.5 Hz for prelimbic cortex. The resulting spectrograms were averaged and displayed. To statistically compare spectrograms between treatments, a nonparametric permutation test to correct for multiple comparisons with two-tailed pixel-based statistics was computed using 500 permutations and a p-value of 0.05 [36].

To determine the predictive power between brain regions during ripples, the time-frequency Spectral Granger Causality was computed for each directionality [37]. A window with length of 2.2 seconds centered around each ripple peak was extracted for the simultaneous hippocampal and prelimbic cortex signals. The length of this window was chosen to at least capture one cycle of 0.5 Hz activity. A two-second-long time-frequency non-parametric Spectral Granger causality was computed by implementing a Short- time Fourier transform with a 500ms Hanning window with 10ms steps using the Fieldtrip functions ft_freqanalysis and ft_connectivityanalysis respectively. To determine statistical differences between granger spectrograms we created randomized trials by taking 400 random ripples per treatment and computing their time-frequency granger causality as described above. The result was stored, and the procedure was repeated 30 times to give a total of 30 randomized trials per treatment. We then used the trials of the rgs14 and control treatments to determine significant statistical difference in each pixel of the time-frequency matrix by

721 applying a nonparametric permutation test to correct for multiple comparisons with a two-tailed pixel-based
722 correction, using 500 permutations and a p-value of 0.05.

723 ### *Neuronal activity analysis*

724 #### *Spike sorting*
725 An important step of our analysis was identifying the cortical neurons and their spiking activity. The
726 sleep and trial recordings of each tetrode of the prelimbic cortex were extracted and concatenated
727 chronologically to allow tracking the individual neuronal activity across the whole study day. The tetrode
728 recordings were preprocessed by applying a bandpass filter between 300 and 3000 Hz. For each tetrode,
729 multiple spike sorting algorithms were run using the SpikeInterface python-based framework [38]. The spike
730 sorters used were Tridesclous, SpikingCircus, Klusta, HerdingSpikes, Ironclust, and MountainSort4. The
731 default parameters included in SpikeInterface per spike sorter were used. Agreement between the spike
732 sorters was computed and only putative neurons that were detected by at least two spike sorters were
733 considered. When a tetrode didn't have any consensus, the detections of the MountainSort4 spike sorter
734 were used given that this spike sorter had better scores according to the SpikeForest [39] metrics and our
735 own examinations. After the putative neurons were detected, an experienced user curated manually the
736 detections by visual inspection using the Phy interface and labeled them as either good, multiunit activity,
737 or noise.
738

739 #### *Waveform extraction*
740 Sampled at 30 kHz, the prelimbic cortex tetrode channels were loaded and then filtered using a 3rd
741 order Butterworth bandpass filter with a frequency range of 300-600 Hz. Neurons labelled as 'good' were
742 used for further analysis. A preliminary waveform per neuron was defined with an 82-sample window with
743 40 samples before and 41 samples after the spike timestamp (ST). For each neuron, STs were randomly
744 permuted and a total of 2000 were selected. The permutation was done in order to avoid bias when
745 selecting waveforms. These 2000 waveforms were averaged to obtain the mean spike waveform per
746 neuron. Since tetrodes were used to record neuronal activity during the task and sleep, there were 4
747 average waveforms to choose from. The one with the highest peak amplitude was chosen. For each neuron,
748 all STs were stored. Further, each neuron was assigned a unique ID. This process was performed for all
749 neurons of all rats.
750

751 #### *Neuron classification*
752 The average neuron waveforms calculated from rats 1, 2, 6 and 9 were categorized as 'Vehicle' and
753 stored in a 139 (t1) × 82 matrix, with 139 being the total number of putative neurons and 82 being the
754 number of samples as mentioned before. Similarly, 'RGS14' data from rats 3, 4, 7, 8 was stored as a 353
755 (t2) × 82 matrix. Variables t1 and t2 were the total counts of neurons for the respective treatments. The
756 bz_CellClassification.m script from Buzsaki lab's GitHub was used to compute the trough-to-peak delay
757 time and the spike width for the spike waveform of each putative neuron. The function
758 ClusterPointsBoundaryOutBW.m of the same repository was modified to incorporate visualization of
759 interneuron and pyramidal data for both treatments. Neurons were then visualized in a 2D plane with x and
760 y axes as trough-to-peak delay and spike width respectively. The set of coordinates of all putative neurons
761 were fed into a Gaussian Mixture Model (GMM) with two components in order to find the centroids of the
762 clusters of pyramidal cells and interneurons. The cluster which contained spikes with high values of spike
763 width and trough-to-peak delay was labelled as the pyramidal neurons cluster, while the remaining one was
764 labelled as the interneurons cluster. For both clusters, a threshold of mean +/- 2 SD with respect to their
765 centroids was used to filter out the outliers. Next, the firing rates of the remaining neurons were calculated
766 as is described in the following paragraph and those with extreme firing rate values were reinspected in the
767 Phy interface by another experimenter to potentially discard remaining false positives. After this procedure
768 there were a total of 101 pyramidal neurons for the RGS14 treatment and 57 for Vehicle. The total number

769 of interneurons were 18 for RGS14 and 7 for Vehicle. In the following analyses, only pyramidal neurons
770 were used given the low number of interneurons detected.
771

Firing rate analysis

773 The spikes of each neuron were grouped by the sleep stage during which they fired. The total number
774 of spikes of a neuron during a specific sleep stage were determined by counting all the spikes occurring
775 during the sleep stage in question across pre-trial sleep, post-trial sleep and trials periods of a single day.
776 The cumulative amount of time spent in a specific sleep stage during the day was determined similarly.
777 Using these two values, the firing rate of a neuron during a sleep stage was computed by dividing the total
778 number of spikes during the sleep stage by the cumulative amount of time spent in seconds in the sleep
779 stage. The firing rate during each sleep and wake stage was calculated for all neurons. The firing rates of
780 neurons during the 'Wake' stage in the vehicle control condition were divided into 5 quantiles based on their
781 magnitudes (0-20%, 20-40%, 40- 60%, 60-80%, 80-100%), as shown in **Figure 2G**. The upper-limit values
782 of firing rate differentiating the groups in Vehicle were then used as a threshold to divide the neurons in the
783 RGS treatments in 5 groups as well. The spike timestamps during NonREM sleep were collected across
784 the whole study day for each neuron and the corresponding slow oscillation phases during each spike
785 timestamps were extracted. The slow oscillation phase during spikes was calculated as described above
786 for ripples and spindles.
787

Cortical activity during ripples

789 Using the spike timestamps during NonREM sleep, the cortical pyramidal neuron response to
790 hippocampal ripples was computed in a 2 second window defined around the peak of each ripple. For each
791 ripple the activity of all pyramidal neurons detected during that day was extracted. The spikes timestamps
792 in the 2 second window were normalized to vary from -1 to 1 seconds, where 0 was the ripple peak. After
793 concatenating the normalized timestamps across all ripple-centered windows per neuron, they were binned
794 in 10 ms bins and the number of spikes was determined for each bin. Hence, for each neuron, a [1 x 200]
795 column vector was obtained. This vector was then z-normalized. The final z-scored vector was found by
796 averaging the z-scored vector over all neurons. The data was smoothed twice using the MATLAB smooth
797 function. To visualize the activity of prelimbic cortex pyramidal neurons around the ripple, the firing activity
798 of a neuron was determined from a 50 ms window around the peak of the ripple (-20 to +30 ms) by
799 quantifying the number of spikes. After compiling the firing activity around the ripple peak for each neuron
800 the values were sorted in an ascending order and was visualized using the MATLAB imagesc function.
801

Figures

803 Figures were generated in GraphPad Prism (truncated violin plots with high smoothing).
804

Author contributions: Conceptualization: LG, INL, Methodology: LG, INL, ZK, MK, Investigation: INL, MK, AS, JvdM, AIA, Data analysis: AAZ, AR, MK, MB, SN, Funding acquisition: LG, INL, Writing – original draft: LG, Writing – review & editing: INL, MK, ZK

Competing interests: Authors declare that they have no competing interests.

**Data and materials availability:** All data is available on the Donders Repository, code on GitHub (see materials and methods for links)

Increasing cortical plasticity leads to memory interference and enhanced hippocampal-cortical interactions - Supplementary Materials

Irene Navarro-Lobato[1]*, Adrian Aleman-Zapata[1], Anumita Samanta[1], Milan Bogers[1], Shekhar Narayanan[1], Abdelrahman Rayan[1], Alejandra Alonso[1], Jacqueline van der Meij[1], Mehdi Khamassi[2], Zafar Khan[3], Lisa Genzel[1]*
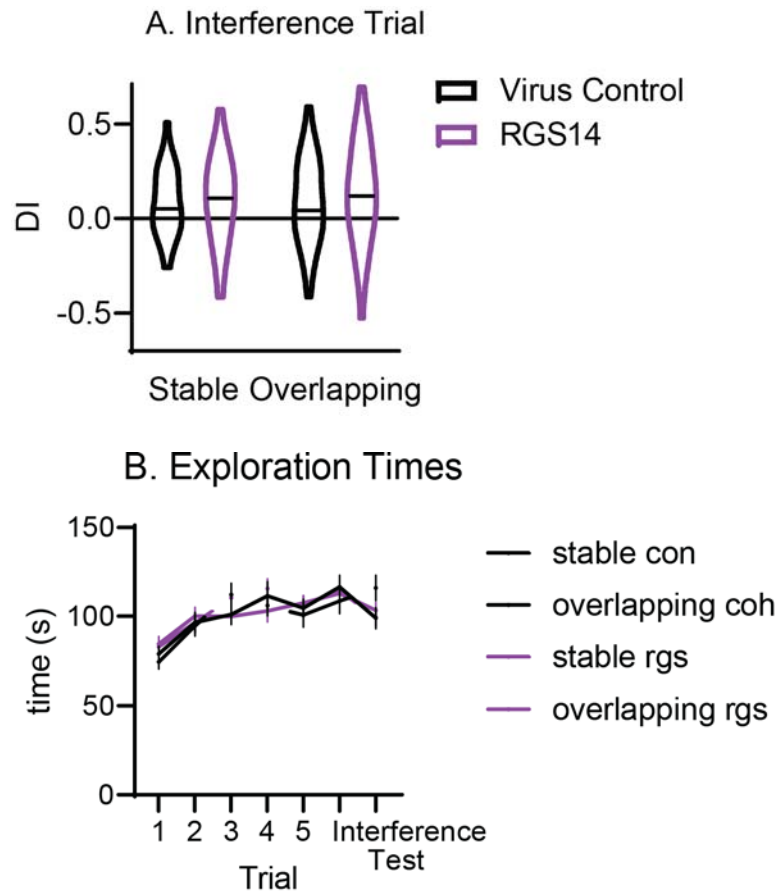
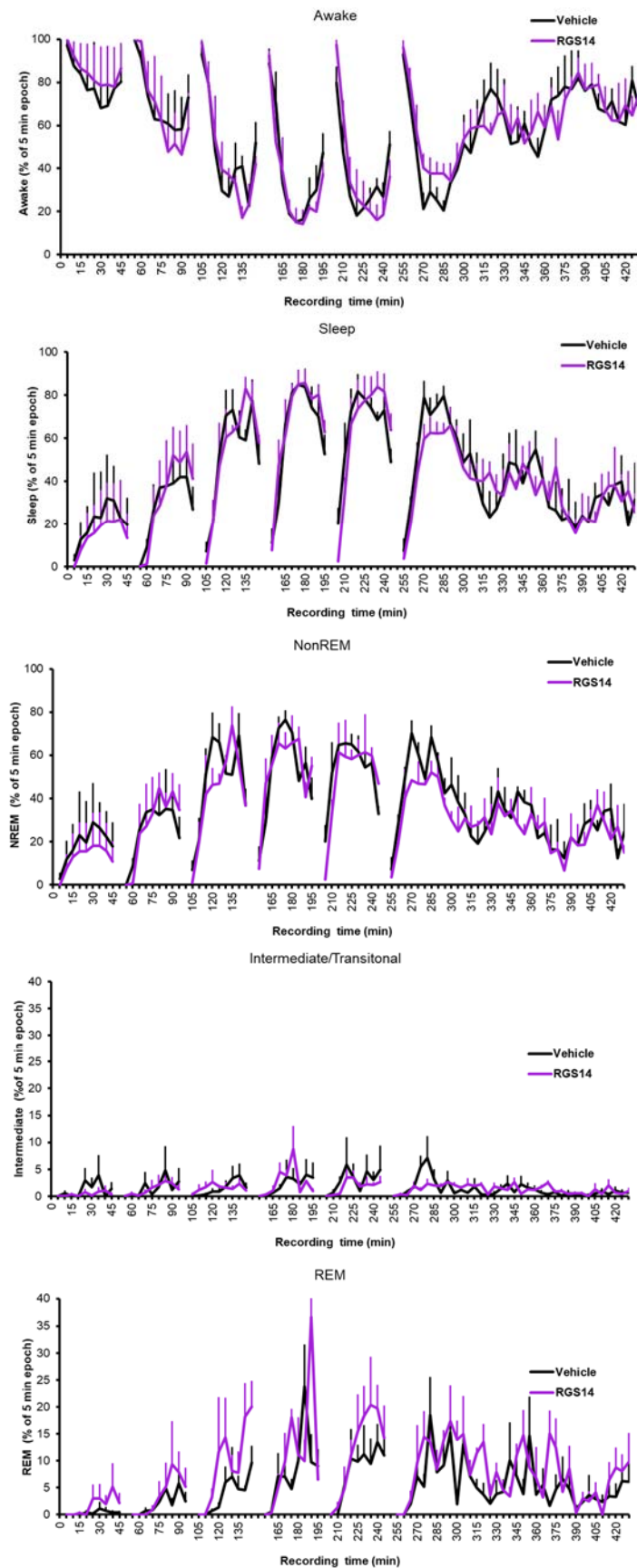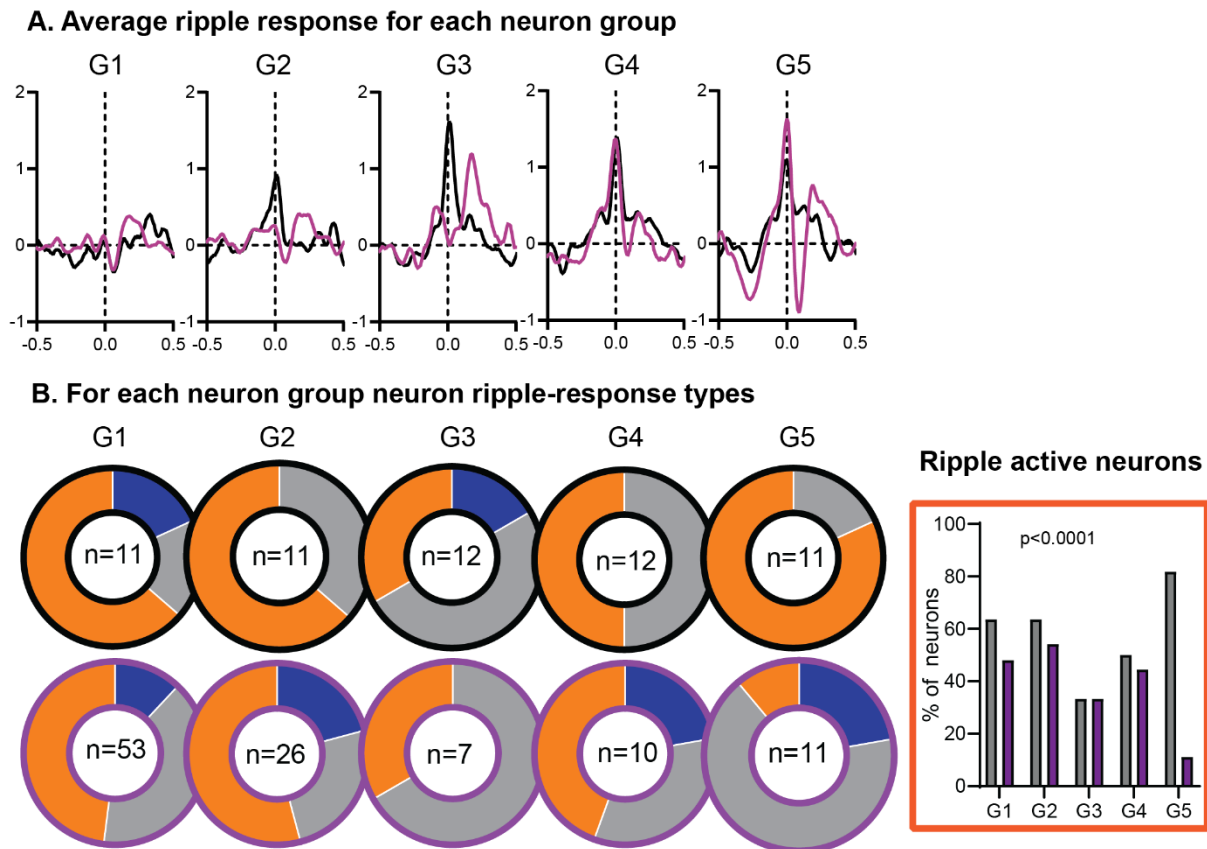Fig.S1: A. Discrimination Index for the interference trial. B. Exploration times for all trials and conditions

Fig. S2: Wake and sleep states for each 5 min bin the sleep recording box. Averaged across conditions, SEM calculated with n=animal

A. Oscillation Characteristics

B. Firing rate changes across states

Fig. S3: A. intrinsic frequency of Delta waves and spindles. Spindle Rate and Amplitude as well as SO coupling. B. Average firing rate per neuron group (1-5) and consciousness state. Quiet wake is wake in the sleep recording box, microarousal is wake < 15s in the sleep recording box.

A. Average ripple response for each neuron group

B. For each neuron group neuron ripple-response types

Fig. S4: A. Average neuronal firing (z-normalized activity) with 0 time of ripple, split for firing-rate neuron groups. B. Classification into ripple-supressed (blue), ripple-neutral (grey) and ripple-active (orange) neurons per firing rate group. On the right ripple active neurons per neuron group. There was a significant effect where in RGS there are less G5 neurons that are ripple active.
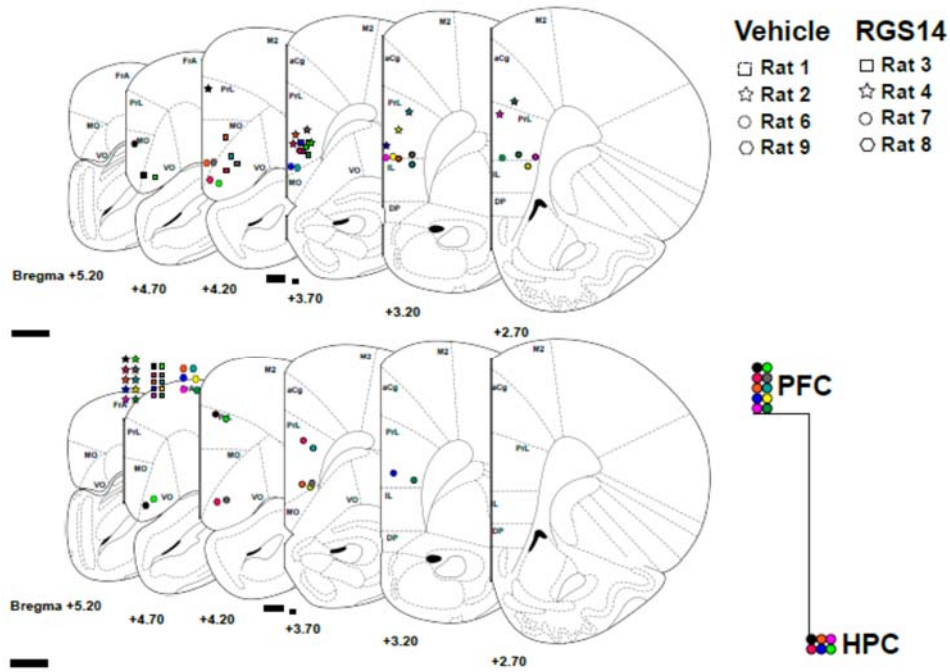
850
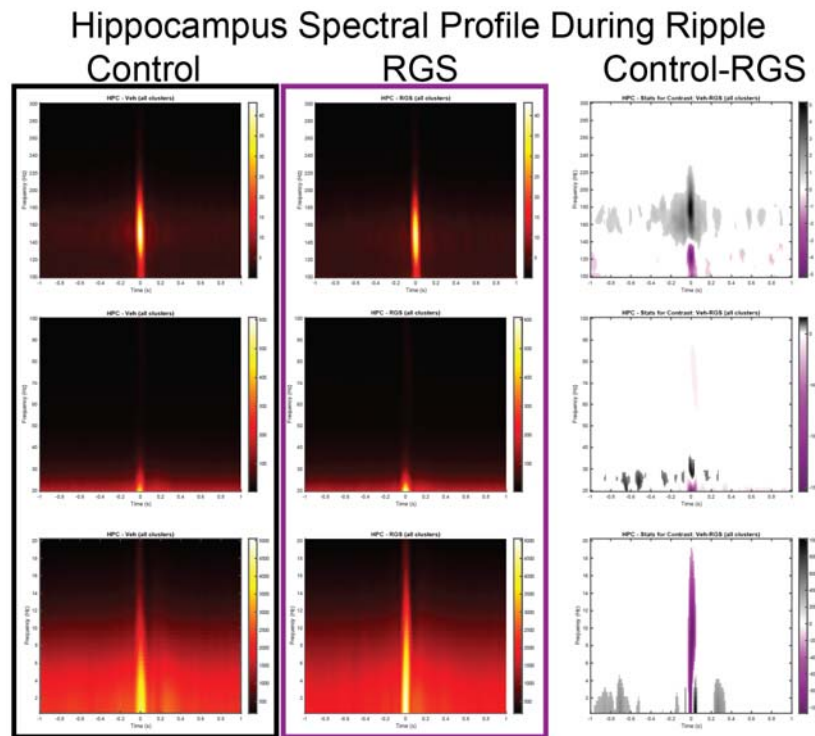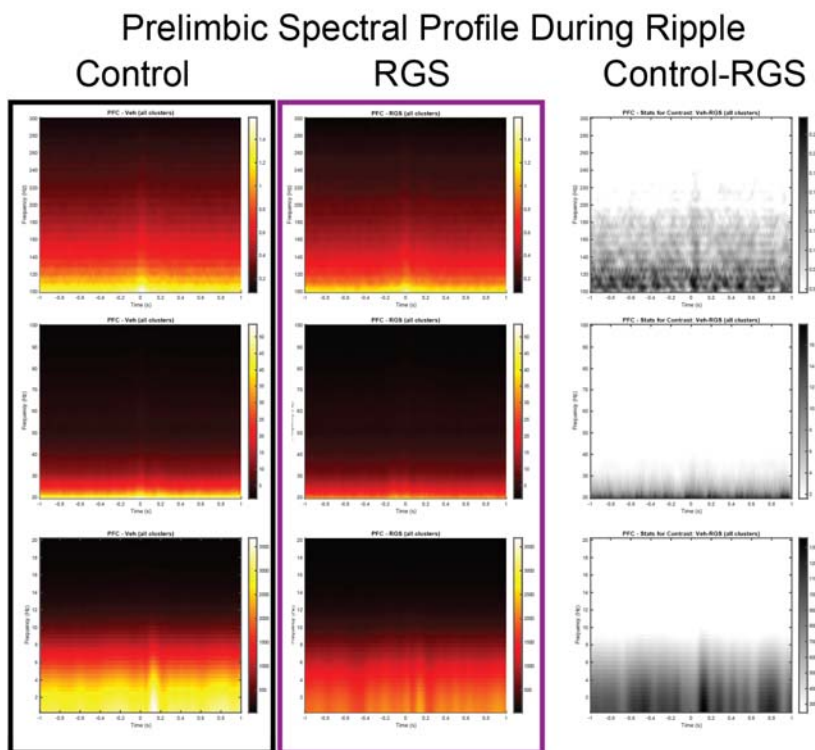851   Fig. S5: Placement of tetrodes per rat and brain area.
852

Fig. S6 Hippocampal (top) and prelimbic (bottom) spectral profile around ripple events for control animals (black) and RGS14 (purple) and the contrast (pixel-based correction for multiple comparison). Purple RGS14 higher, grey Control higher. From top to bottom windows 100-300Hz, 20-100 Hz and 0-20Hz.
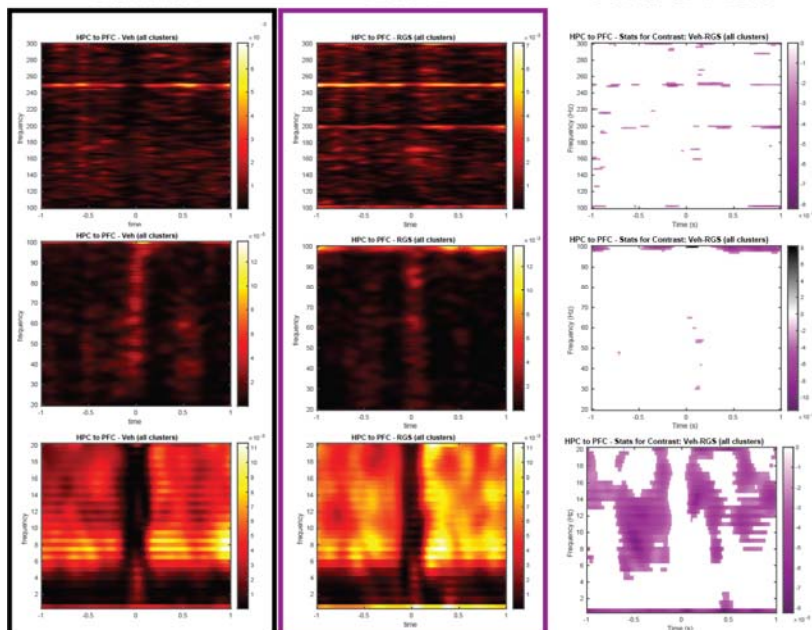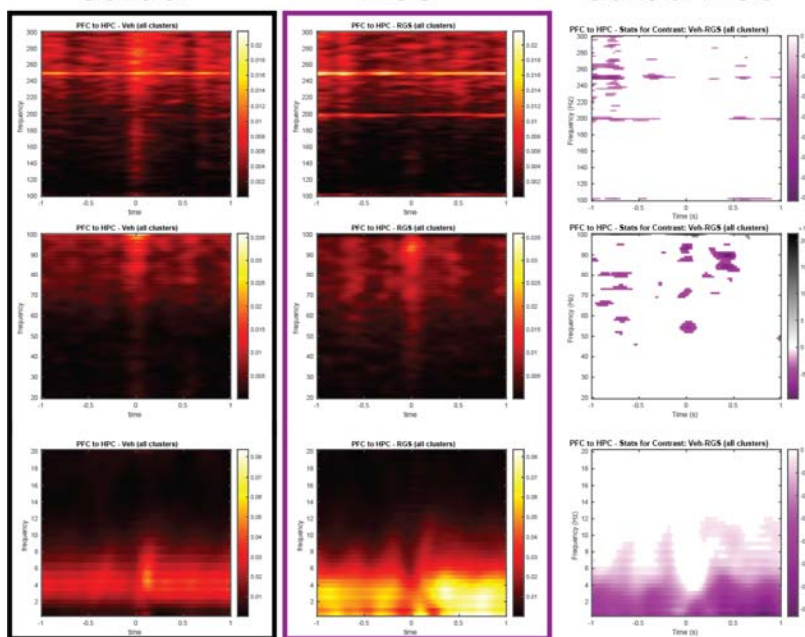
Fig. S7 Hippocampal to prelimbic (top) and prelimbic to hippocampus (bottom) granger time frequency analysis around ripple events for control animals (black) and RGS14 (purple) and the contrast (pixel-based correction for multiple comparison). Purple RGS14 higher, grey Control higher. From top to bottom windows 100-300Hz, 20-100 Hz and 0-20Hz.

1   Scoville, W. & Milner, B. Loss of recent memory after bilateral hippocampal lesions. *J Neurol Neurosurg Psychiat* **20**, 11-23 (1957).

2   Marr, D. A theory for cerebral neocortex. *Proc R Soc Lond B Biol Sci* **176**, 161-234 (1970).

3   McClelland, J. L., McNaughton, B. L. & O'Reilly, R. C. Why there are complementary learning systems in the hippocampus and neocortex: insights from the successes and failures of connectionist models of learning and memory. *Psychol Rev* **102**, 419-457 (1995).

4   Marr, D. Simple memory: a theory for archicortex. *Philos Trans R Soc Lond B Biol Sci* **262**, 23-81 (1971).

5   Navarro-Lobato, I. *et al.* 14-3-3ζ is crucial for the conversion of labile short-term object recognition memory into stable long-term memory. *Journal of neuroscience research* **99**, 2305-2317, doi:10.1002/jnr.24894 (2021).

6   Masmudi-Martín, M. *et al.* RGS14(414) treatment induces memory enhancement and rescues episodic memory deficits. *Faseb j* **33**, 11804-11820, doi:10.1096/fj.201900429RR (2019).

7   Navarro-Lobato, I. *et al.* RGS14414-Mediated Activation of the 14-3-3ζ in Rodent Perirhinal Cortex Induces Dendritic Arborization, an Increase in Spine Number, Long-Lasting Memory Enhancement, and the Prevention of Memory Deficits. *Cerebral Cortex* **32**, 1894-1910, doi:10.1093/cercor/bhab322 (2021).

8   Masmudi-Martín, M. *et al.* Reversal of Object Recognition Memory Deficit in Perirhinal Cortex-Lesioned Rats and Primates and in Rodent Models of Aging and Alzheimer's Diseases. *Neuroscience* **448**, 287-298, doi:https://doi.org/10.1016/j.neuroscience.2020.08.039 (2020).

9   López-Aranda, M. F. *et al.* Role of Layer 6 of V2 Visual Cortex in Object-Recognition Memory. *Science* **325**, 87-89, doi:doi:10.1126/science.1170869 (2009).

10   Genzel, L. *et al.* The object space task shows cumulative memory expression in both mice and rats. *PLoS Biol* **17** (2019).

11   Tononi, G. & Cirelli, C. Sleep and the Price of Plasticity: From Synaptic and Cellular Homeostasis to Memory Consolidation and Integration. *Neuron* **81**, 12-34 (2014).

12   Tononi, G. & Cirelli, C. Sleep function and synaptic homeostasis. *Sleep Medicine Reviews* **10**, 49-62, doi:10.1016/j.smrv.2005.05.002 (2006).

13   Huber, R., Ghilardi, M. F., Massimini, M. & Tononi, G. Local sleep and learning. *Nature* **430**, 78-81 (2004).

14   Grosmark, A. D. & Buzsaki, G. Diversity in neural firing dynamics supports both rigid and learned hippocampal sequences. *Science* **351**, 1440-1443 (2016).

15   Buzsaki, G. Two-stage model of memory trace formation: A role for "noisy" brain states. *Neuroscience* **31**, 551-570 (1989).

16   Benchenane, K. *et al.* Coherent theta oscillations and reorganization of spike timing in the hippocampal- prefrontal network upon learning. *Neuron* **66**, 921-936, doi:10.1016/j.neuron.2010.05.013 (2010).

17   Genzel, L., Kroes, M. C. W., Dresler, M. & Battaglia, F. P. Light sleep versus slow wave sleep in memory consolidation: a question of global versus local processes? *Trends in Neurosciences* **37**, 10-19 (2014).

18   Molle, M., Marshall, L., Gais, S. & Born, J. Grouping of spindle activity during slow oscillations in human non-rapid eye movement sleep. *The Journal of neuroscience : the official journal of the Society for Neuroscience* **22**, 10941-10947 (2002).

19   Peyrache, A., Khamassi, M., Benchenane, K., Wiener, S. I. & Battaglia, F. P. Replay of rule-learning related neural patterns in the prefrontal cortex during sleep. *Nat Neurosci* **12**, 919-926 (2009).

20   Maingret, N., Girardeau, G., Toderova, R., Goutiere, M. & Zugaro, M. Hippocampo-cortical coupling mediates memory consolidation during sleep. *Nature Neuroscience* **19**, 959-964, doi:10.1038/nn.4304 (2016).

21   Sirota, A., Csicsvari, J., Buhl, D. & Buzs+¡ki, G. r. Communication between neocortex and hippocampus during sleep in rodents. *Proceedings of the National Academy of Sciences* **100**, 2065-2069 (2003).

22   Diekelmann, S. & Born, J. The memory function of sleep. *Nat Rev Neurosci* **11**, 114-126 (2010).

23   Buzsaki, G. Hippocampal sharp wave-ripple: A cognitive biomarker for episodic memory and planning. *Hippocampus* **25**, 1073-1188, doi:10.1002/hipo.22488 (2015).

24   Girardeau, G., Benchenane, K., Wiener, S. I., Buzs ki, G. & Zugaro, M. B. Selective suppression of hippocampal ripples impairs spatial memory. *Nat Neurosci* **12**, 1222-1223 (2009).

25   Wierzynski, C. M., Lubenov, E. V., Gu, M. & Siapas, A. G. State-dependent spike-timing relationships between hippocampal and prefrontal circuits during sleep. *Neuron* **61**, 587-596, doi:10.1016/j.neuron.2009.01.011 (2009).

26   Rothschild, G., Eban, E. & Frank, L. M. A cortical-hippocampal-cortical loop of information processing during memory consolidation. *Nat Neurosci* **20**, 251-259 (2017).

27   Wang, D. V. & Ikemoto, S. Coordinated Interaction between Hippocampal Sharp-Wave Ripples and Anterior Cingulate Unit Activity. *The Journal of neuroscience : the official journal of the Society for Neuroscience* **36**, 10663-10672, doi:10.1523/JNEUROSCI.1042-16.2016 (2016).

28   Lopez-Aranda, M. F. *et al.* Role of layer 6 of V2 visual cortex in object-recognition memory. *Science* **325**, 87-89, doi:10.1126/science.1170869 (2009).

29   Masmudi-Martin, M. *et al.* RGS14414 treatment induces memory enhancement and rescues episodic memory deficits. *FASEB J* **33**, 11804-11820, doi:10.1096/fj.201900429RR (2019).

30   Brunetti, P. M. *et al.* Design and fabrication of ultralight weight, adjustable multi-electrode probes for electrophysiological recordings in mice. *J Vis Exp*, e51675, doi:10.3791/51675 (2014).

31   Kloosterman, F. *et al.* Micro-drive array for chronic in vivo recording: drive fabrication. *J Vis Exp*, doi:10.3791/1094 (2009).

32   Nguyen, D. P. *et al.* Micro-drive array for chronic in vivo recording: tetrode assembly. *J Vis Exp*, doi:10.3791/1098 (2009).

33   Paxinos, G. W., Charles. *The Rat Brain Atlas in Stereotaxic Coordinates*. 7th Edition edn, (Academic Press, 2013).

34   Genzel, L. *et al.* The object space task shows cumulative memory expression in both mice and rats. *PLoS Biol* **17**, e3000322, doi:10.1371/journal.pbio.3000322 (2019).

35   Oostenveld, R., Fries, P., Maris, E. & Schoffelen, J. M. FieldTrip: Open source software for advanced analysis of MEG, EEG, and invasive electrophysiological data. *Comput Intell Neurosci* **2011**, 156869, doi:10.1155/2011/156869 (2011).

36   Maris, E. & Oostenveld, R. Nonparametric statistical testing of EEG- and MEG-data. *Journal of Neuroscience Methods* **164**, 177-190, doi:https://doi.org/10.1016/j.jneumeth.2007.03.024 (2007).

973　37　Dhamala, M., Rangarajan, G. & Ding, M. Analyzing information flow in brain networks
974　　　with nonparametric Granger causality. *NeuroImage* **41**, 354-362,
975　　　doi:https://doi.org/10.1016/j.neuroimage.2008.02.020 (2008).
976　38　Buccino, A. P. *et al.* SpikeInterface, a unified framework for spike sorting. *eLife* **9**,
977　　　e61834, doi:10.7554/eLife.61834 (2020).
978　39　Magland, J. *et al.* SpikeForest, reproducible web-facing ground-truth validation of
979　　　automated neural spike sorters. *eLife* **9**, e55167, doi:10.7554/eLife.55167 (2020).
980

981

982